Computers and Geotechnics 166 (2024) 106037

Contents lists available at ScienceDirect

Computers and Geotechnics

journal homepage: www.elsevier.com/locate/compgeo

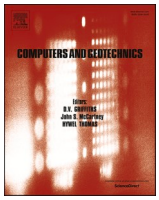

# Random field failure and post-failure analyses of vertical slopes in soft clays

Samzu Agbaje [a], Xue Zhang [a,*], Edoardo Patelli [b], Darren Ward [c], Luisa Dhimitri [c]

[a] Department of Civil and Environmental Engineering, University of Liverpool, Liverpool, UK
[b] Centre for Intelligent Infrastructure, University of Strathclyde, Glasgow, UK
[c] In Situ Site Investigation, East Sussex, UK

ARTICLE INFO

*Keywords:*
Soft clay
Spatial variability
Random field analysis
Slope stability
Post-failure analysis

ABSTRACT

This research investigates the spatial heterogeneity of cohesion within soft clay and its implications for slope stability and post-failure analysis. In-situ cone penetration tests were conducted in alluvial soft clays to calibrate probabilistic strength properties. Slope stability analyses employed deterministic, semi-deterministic, and comprehensive probabilistic approaches, while post-failure analysis utilised the nodal integration-based particle finite element method. The undrained shear strength ($c_u$) demonstrated a log-normal distribution (mean: 19 kPa, standard deviation: 3 kPa), with correlation lengths modeled through Bayesian inference. Treating correlation lengths as distributions resulted in a negligible 2% difference compared to using a single value for the probability of failure. Semi-deterministic analyses exhibited results similar to probabilistic analyses, offering computational advantages. Nevertheless, probabilistic analysis, considering spatial variability, provided more comprehensive insights for post-failure analysis. For a vertical slope of critical height in the studied soft clay, probabilistic analyses predicted a range of runout distances from 0 m to over 125 m. Specifically, 89% of these distances were less than 80 m, and 82% were less than 40 m. The findings contribute to an enhanced understanding of spatial variations in soil strength within soft clay slopes, providing valuable insights for future geotechnical assessments and design considerations.

## 1. Introduction

Alluvial soil is a common type of soft clay found worldwide in areas where rivers or other bodies of water are present. The characteristics of alluvium, including its texture and particle size distribution, are heavily influenced by the energy levels of the depositional environment. In low-energy environments, clay and silt particles are predominantly deposited, while high-energy environments can transport larger particles such as sand and gravel, resulting in significant spatial variability in the shear strength of alluvial soils.

Given the spatial variability of shear strength, designing geostructures in locations with soft clays, such as alluvial soils, presents a significant challenge. The current stability analysis of geostructures heavily relies on deterministic analysis, often resulting in solutions that are either unsafe or overly conservative. To address this issue, geotechnical design codes, such as Eurocode 7, employ the partial factor approach to account for spatial variability. This approach involves applying a partial factor to soil strength to reflect uncertainty. However, relying solely on the partial factor approach cannot capture the complete range of soil strength variability, and its reliability is still a subject of debate. Incorporating the spatial variability of soil properties is a complex task that requires careful consideration of multiple factors, including computationally intensive stochastic modelling techniques and accurate, representative data on soil properties.

Random field analysis (RFA) is a powerful tool used to investigate uncertainties in geotechnical design. By employing statistical principles and stochastic models, RFA provides insights into the random behaviour of soil parameters and predicts the response of soil structures under uncertain conditions. The Random Finite Element Method (RFEM) combines RFA with finite element analysis and has been applied to various geotechnical problems involving soils with spatial variability. Studies utilising RFEM have examined diverse geotechnical issues, including the bearing capacity of foundations (Li et al., 2015, Selmi et al., 2019, Yi et al., 2020), seepage analysis (Griffiths et al., 1997, Tan et al., 2017), slope stability (Agbaje et al., 2022, Dyson et al., 2019, Jiang et al., 2018), and others.

Despite these contributions, many questions remain unanswered when considering the spatial variation of strength in the analysis of natural slopes. One crucial factor in RFA is the correlation length, which indicates the spatial correlation of a soil parameter. Determining the

* Corresponding author.
*E-mail address:* xue.zhang2@liverpool.ac.uk (X. Zhang).

https://doi.org/10.1016/j.compgeo.2023.106037
Received 10 August 2023; Received in revised form 3 December 2023; Accepted 19 December 2023
Available online 28 December 2023

correlation length through site investigations is not straightforward. Deterministic formulas, such as the one proposed by (DeGroot et al., 1993), may not adequately account for the inconsistent and random occurrence of small changes in soil types within a study area. These changes could include transitions from clay to sand or variations in soil properties due to the presence of impurities like organic content. Given these considerations, a fundamental question arises: Should the correlation length be treated as a variable in space, or is it appropriate to adopt a single mean value for the correlation length? Furthermore, due to the significant time consumption associated with RFA, it is worthwhile to investigate its performance for achieving optimised results. One aspect that merits exploration is the trade-off between safety and speed when comparing deterministic and probabilistic analyses. Conducting a review to assess the effectiveness of the partial factor method proposed by Eurocode 7 will also provide valuable insights. Additionally, the application of random field analysis in slope analysis is primarily focused on the failure stage, specifically the calculation of the factor of safety for a slope. However, limited contributions exist regarding the post-failure stage (Chen et al., 2021, Liu et al., 2021, Ma et al., 2022), particularly in studying the final run-out distance of an unstable slope. Questions regarding the influence of a random field on the run-out distance are still being investigated. This aspect is particularly important as it pertains to the placement of critical infrastructures such as railways, roads, etc., which require a safe distance from potential landslide areas.

In this paper, we address these inquiries by conducting a comprehensive process of RFA on a vertical cutting slope in soft clay. Vertical slopes are commonly encountered, for example, during site investigations involving trial pit excavations. They also arise in earthwork projects where slope benching is performed, as seen in the remediation of soft clay slopes. In both scenarios, engineers must determine a safe vertical height for the excavation without incurring additional costs or necessitating additional land space. Our investigation encompasses the following key steps: First, we gather site-specific data necessary for generating random fields for soft clay ground. Next, we thoroughly analyse the date for calibrating the probabilistic properties of undrained shear strength of the soft clay, with particular emphasis on determining the Correlation Length (CL). Subsequently, we integrate random field generation with the mixed limit analysis method and the Nodal integration-based Particle Finite Element Method (N-PFEM) for conducting slope stability analysis and post-failure analysis. We further compare the results obtained from deterministic analysis, semi-deterministic analysis, and comprehensive probabilistic analysis to gain insights and make meaningful comparisons.

The subsequent sections of the paper are structured as follows: Section 2 introduces the analysis methods adopted in this study. Section 3 details the site investigation, focusing on the calibration of the probabilistic properties of undrained shear strength. Section 4 covers the generation of random fields, while Section 5 presents the simulation results and subsequent discussion. The final conclusions are drawn in Section 6.

## 2. Random field analysis using Monte Carlo simulation

This study investigates the impact of soil strength variability on the stability and the post-failure process of a vertical slope in soft clay. The analysis incorporates random field analysis through Monte Carlo simulation. This section provides a brief overview of the approaches used.

### 2.1. Monte Carlo simulation

Traditional slope stability analyses rely on single-valued parameters, offering deterministic estimates that overlook soil property variability. Acknowledging the probabilistic nature of slope stability is crucial. This study emphasises spatial variations in undrained shear strength in soft clay and their influences on slope failure. By utilising Monte Carlo simulations, we sample a random shear strength, incorporating it into stability and post-failure analyses for a comprehensive understanding.

Various advanced Monte Carlo sampling methods, such as Markov Chain Monte Carlo (MCMC), Transitional Markov Chain Monte Carlo (TMCMC), and Sequential Monte Carlo methods, have been developed. TMCMC has found applications in geotechnical problems, including characterising the statistical uncertainties of spatial variability parameters based on CPT (Ching et al., 2016) and analysing the creep behavior of soft soil and its associated uncertainty (Zhou et al., 2018). In this study, we adopted the recently developed Transitional Ensemble Markov Chain Monte Carlo (TEMCMC) method (Lye et al., 2022) for sampling. Combining the advantages of TMCMC and the Affine-invariant Ensemble sampler, TEMCMC has demonstrated superior performance, requiring less time while maintaining well-moderated acceptance rates within optimal bounds. For more details on the sampling approach used, readers are referred to the work of Lye et al. (2022).

### 2.2. Bayesian inference

Bayesian Inference was employed in this study to derive possible correlation functions for the survey data, allowing the calibration of the correlation length. Bayesian Inference (Lye et al., 2021) is a form of statistical inference based on Bayes theorem, updating prior knowledge as observations are made. Its mathematical formulation is defined as

$$P(\theta|D,M) = \frac{P(D|\theta,M)P(\theta|M)}{P(D|M)} \tag{1}$$

where $\theta$ is the vector of the uncertain parameters to be estimated, $D$ is the vector of the observed or measured data, and $M$ is the model or function that the data follows. The prior distribution, $P(\theta|M)$, characterises the knowledge of the inferred parameter(s) before any measurements are taken. The likelihood function, $P(D|\theta,M)$, accounts for the error in measurements and the agreement between the measurements and model predictions based on the inferred parameters. $P(D|M)$ is the evidence function. The posterior distribution, $P(\theta|D,M)$, reflects updated knowledge after observations are made, with the evidence serving as a normalisation constant that gauges how well the measurements align with the given model. In this study, the model pertains to the correlation functions of the surveyed data. Details on the used Bayesian Inference has been documented by Lye et al. (2021).

### 2.3. Mixed limit analysis for slope stability

Limit analysis is widely applied in slope stability analysis, categorised into three types: the upper bound (kinematical) formulation, the lower bound (static) formulation, and the mixed formulations. The kinematical formulation considers displacement as the sole variable, providing an upper limit for the maximum load. Conversely, the static formulation considers stress as the only variable, resulting in a lower limit for the maximum load. The mixed formulation utilises both displacement and stress as variables. According to (Krabbenhøft et al., 2007, Zhang et al., 2019), a mixed limit analysis formulation can be expressed as a min–max optimisation problem:

$$\begin{aligned} &\min_{\boldsymbol{u}}\max_{(\boldsymbol{\sigma},\alpha)} \quad \alpha + \int_{\Omega} \boldsymbol{\sigma}^T \nabla^T(\boldsymbol{u}) d\Omega - \alpha \int_{\Gamma_t} \bar{\boldsymbol{t}}^T \boldsymbol{u} d\Gamma - \int_{\Omega} \boldsymbol{b}^T \mathbf{u} d\Omega \\ &\text{subject to} \quad f(\boldsymbol{\sigma}) \leq 0 \end{aligned} \tag{2}$$

where $\boldsymbol{\sigma} = \left(\sigma_{xx},\ \sigma_{yy},\ \sigma_{zz},\ \sigma_{yz},\ \sigma_{zx},\ \sigma_{xy}\right)^T$ is the Cauchy stress; $\mathbf{u}$ is the displacement; $\mathbf{b}$ is the body force; $\bar{\boldsymbol{t}}$ is the prescribed traction; $f(\boldsymbol{\sigma})$ is the yield function; $\alpha$ is the collapse load factor meaning $\alpha\bar{\boldsymbol{t}}$ the ultimate force the geostructure can sustain; and $\nabla$ is the differential operator matrix.

Following the study by Meng et al. (2020), a three-node triangular element was employed, and the approximation of displacement ($\boldsymbol{u}$) within an element is expressed as:

$$\boldsymbol{u}(\boldsymbol{x}) \approx \boldsymbol{N}\widehat{\boldsymbol{u}} \tag{3}$$

where $\widehat{\boldsymbol{u}}$ incorporates the displacement values at mesh nodes, and $\boldsymbol{N}$ denotes the shape function. Accordingly, the strain approximation is given by:

$$\boldsymbol{\varepsilon} \approx \nabla^T(\boldsymbol{N}\widehat{\boldsymbol{u}}) = \boldsymbol{B}\widehat{\boldsymbol{u}} \tag{4}$$

where $\boldsymbol{B} = \nabla^T\boldsymbol{N}$ stands for the strain–displacement matrix. Sequentially, the discretisation of the min–max problem (2) takes the form:

$$\begin{aligned} &\min_{\widehat{\boldsymbol{u}}}\max_{(\boldsymbol{\sigma},\alpha)} \quad \alpha + \int_\Omega \boldsymbol{\sigma}^T\boldsymbol{B}d\Omega\widehat{\boldsymbol{u}} - \boldsymbol{\alpha}\int_{\Gamma_t}\bar{\boldsymbol{t}}^T\boldsymbol{N}d\Gamma\widehat{\boldsymbol{u}} - \int_\Omega \boldsymbol{b}^T\boldsymbol{N}d\Omega\widehat{\boldsymbol{u}} \\ &\text{subject to} \quad f(\boldsymbol{\sigma}) \le 0 \end{aligned} \tag{5}$$

where $\boldsymbol{\sigma}$ represents the uniform stress in the element. The analytical resolution of the minimisation component leads to a subsequent maximisation problem:

$$\begin{aligned} &\max_{(\boldsymbol{\sigma},\alpha)} \quad \alpha \\ &\text{subject to}: \int_\Omega \boldsymbol{\sigma}^T\boldsymbol{B}d\Omega = \alpha\int_{\Gamma_t}\bar{\boldsymbol{t}}^T\boldsymbol{N}d\Gamma + \int_\Omega \boldsymbol{b}^T\boldsymbol{N}d\Omega \\ &\quad\quad f(\boldsymbol{\sigma}) \le 0 \end{aligned} \tag{6}$$

To mitigate the volumetric locking issue inherent in three-node triangular elements, nodal integration is implemented based on smoothing domains following the work of Meng et al. (2020). This approach effectively overcomes the volumetric locking issue with linear elements, as demonstrated in the works of Meng et al. (2020) and Zhang et al. (2023).

Subsequent to nodal integration, the maximisation problem (6) is reformulated as

$$\begin{aligned} &\max_{(\boldsymbol{\sigma},\alpha)} \quad \alpha \\ &\text{subject to}: \begin{cases} \overline{\boldsymbol{B}}^T\widehat{\boldsymbol{\sigma}} - \overline{\boldsymbol{F}}_{\mathrm{b}} = \overline{\boldsymbol{F}}_{\mathrm{t}} \\ f^i(\widehat{\boldsymbol{\sigma}}) \le 0 \quad i = 1, 2, \cdots, NN \end{cases} \end{aligned} \tag{7}$$

where the notation $(\bullet)^i$ denotes the value of $(\bullet)$ at the $i$th node unless otherwise specified, and $NN$ represents the total number of nodes. The vector $\widehat{\boldsymbol{\sigma}}$ encompasses stress components at all mesh nodes and can be regarded as the weighted average stress of triangles adjacent to the node. The matrix $\overline{\boldsymbol{B}}$ represents the weighted average of the strain–displacement operator, while $\overline{\boldsymbol{F}}_{\mathrm{t}}$ and $\overline{\boldsymbol{F}}_b$ denote the surface force and body force estimated based on nodal integration, respectively. It is noteworthy that, even in the absence of an upper/lower bound feature in this mixed limit formulation, the solution derived from such analysis often closely approximates to the exact bearing capacity of a structure, as indicated by Nguyen (2023).

### 2.4. N-PFEM for post-failure analysis

The analysis of post-failure processes in slope failure poses a challenge. This is due to the substantial deformation experienced by the sliding soil, resulting in significant mesh distortion when employing the traditional finite element method. In this study, we utilise the N-PFEM developed by Meng et al. (2021) and Zhang et al. (2022) for post-failure analysis. The fundamental steps of the N-PFEM are outlined (see also Fig. 1):

1. Define the computational domain by using the alpha-shape technique with the particle cloud, $P^n$;
2. Generate triangle meshes, $M^{n+1}$, by triangulating the domain based on the particle cloud and the identified domain boundary;
3. Create cells, $C^{n+1}$, corresponding to $M^{n+1}$;

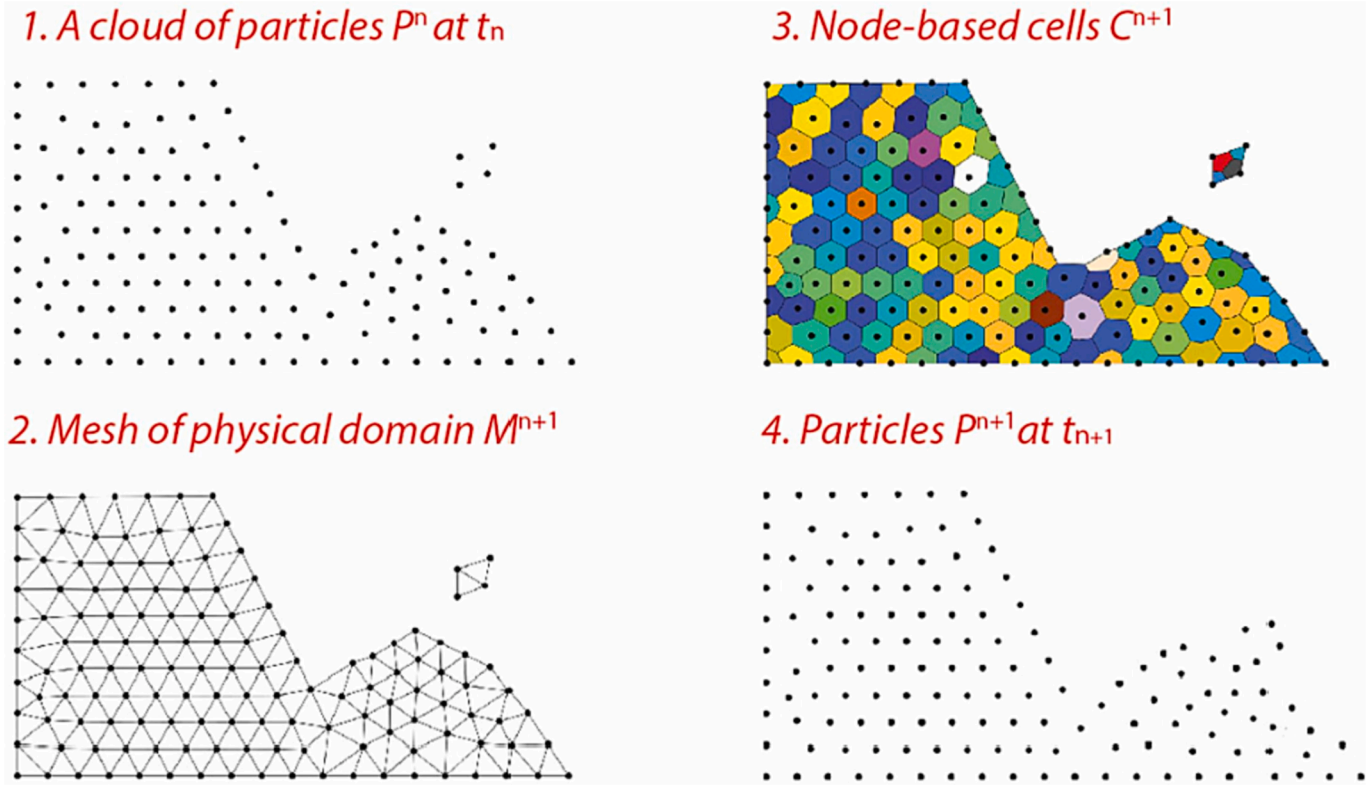


**Fig. 1.** Computational circle of the N-PFEM (after (Zhang et al., 2022)).

4. Solve the governing equations on mesh $M^{n+1}$ and cell $C^{n+1}$;
5. Adjust the positions of the particles (i.e. mesh nodes) based on the resolved incremental displacement and reset the mesh topology to obtain $P^{n+1}$;
6. Iterate through the above process for all time increments.

The N-PFEM combines the advantages of the Lagrangian finite element method in addressing nonlinear problems and meshfree particle methods in dealing with large deformation and free-surface evolution. Its robustness and effectiveness in modelling granular flow and landslide problems have been well demonstrated (Zhang et al., 2023). For more details on the implementation of the utilised N-PFEM, we refer readers to the work of Meng et al. (2021) and Zhang et al. (2022).

## 3. Site investigation survey

Soft clays are commonly encountered in project works undertaken close to rivers, such as earthworks to facilitate road, rail, or coastal development. In this section, we present data collected in the project nearby the Tay River in Perth, Scotland, where alluvial deposits occur. Such soft clays can be found widely across the UK and globally. To better understand the probabilistic strength properties of the soft clays, the data were collected from the Cone Penetration Test (CPT) undertaken by pushing a cone vertically to a maximum depth of 12 m below ground level (bgl). Resistance at the cone tip and around the sleeve at 0.01 m depth intervals was measured. Such semi-continuous data per CPT test is ideal for determining the vertical correlation length. For calibrating the horizontal correlation length, the CPT locations were also positioned in a horizontal alignment along the riverbank, as shown in Fig. 2. A total of 19 CPTs were conducted along a chainage of 505 m. CPT data are provided as supplementary materials of this paper.

The soil was classified according to the Soil Behaviour Type (SBT) Index (Robertson et al., 1983a, Robertson et al., 1983b) - a calibrated relationship between the CPT cone resistance, skin friction, and the type of soils. The pi-chart shown in Fig. 3 indicates that 77.3% of the soils are predominantly cohesive (i.e., clays to silty clays or organic soils) with only 22.7% being granular (i.e., sands). Design standards (BSI, 2015) recommend that any soils with greater than 25% clays should be analysed based on the undrained properties. Hence, the Tresca model was adopted in the following to describe the soil behaviour.

### 3.1. Undrained shear strength

Fig. 4 shows a deterministic representation of the soil behaviour types between chainages 0 + 025 m and 0 + 505 m. The representation was generated based on a simple interpolation between known values. Probabilistic visualisations will be presented later in this paper.

The representation shows that, as is typical for alluvial soils, certain discrete locations of sand deposits exist. To consider the influence of the sand deposits on the CPT interpretation of the undrained shear strength ($c_u$), two sets of interpretation have been undertaken: (i) $c_u$ at all locations (including those with sand deposits); and (ii) $c_u$ at locations with only cohesive soils (i.e., SBT from 1 to 4 only). The interpretation was based on (Lunne et al., 2002):

$$c_u = \frac{q_t - \sigma_{vo}}{N_{kt}} \tag{8}$$

where $q_t$ is the cone tip resistance (corrected for unequal end area effects), $\sigma_{vo}$ is the total overburden stress, and $N_{kt}$ is an empirical cone factor usually in the range from 10 to 20. In this study, a median value of $N_{kt} = 15$ was used.

As we concentrate on soft clays, only data at locations without sand deposits or over-consolidation are utilised in the following analyses. As shown in Fig. 5, the undrained shear strength of the soils statistically varies from 0 to 657 kPa, with the majority having undrained shear strength less than 19 kPa. The distribution type (i.e., a normal or log-normal distribution) the soil parameter obeys was calibrated by measuring the skewness and kurtosis values:

$$\text{Skewness} = \frac{1}{N}\sum_{i=1}^{n}\left[\frac{c_{ui} - \mu_{c_u}}{\sigma_{c_u}}\right]^3 \tag{9}$$

$$\text{Kurtosis} = \frac{1}{N}\sum_{i=1}^{n}\left[\frac{c_{ui} - \mu_{c_u}}{\sigma_{c_u}}\right]^4 \tag{10}$$

where $\mu_{c_u}$ and $\sigma_{c_u}$ are the mean and the standard deviation of $c_u$,

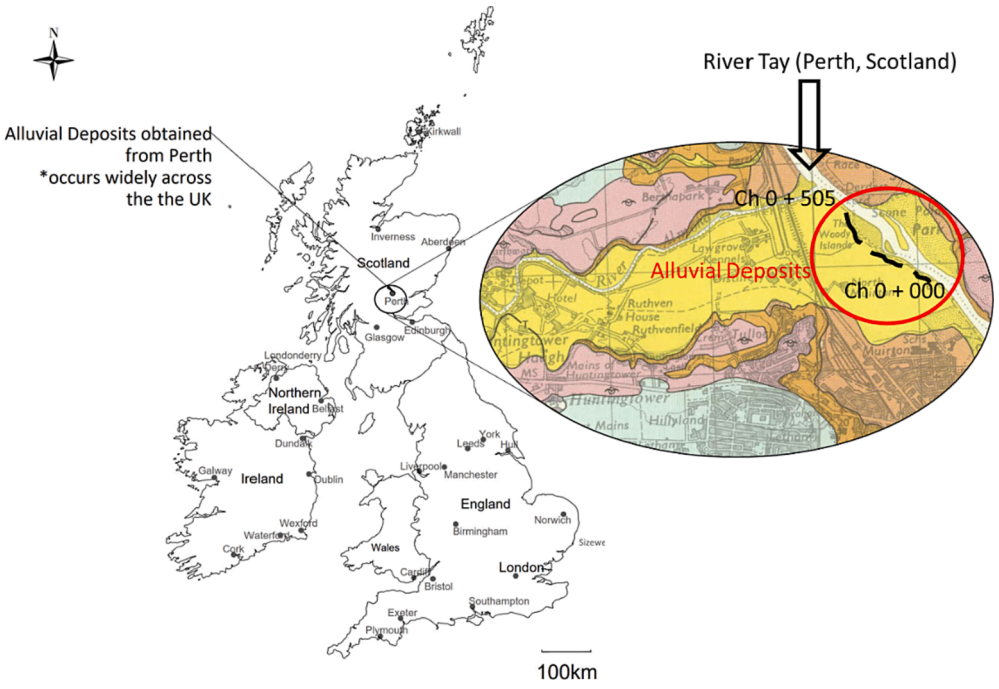


**Fig. 2.** Location of site investigation survey.

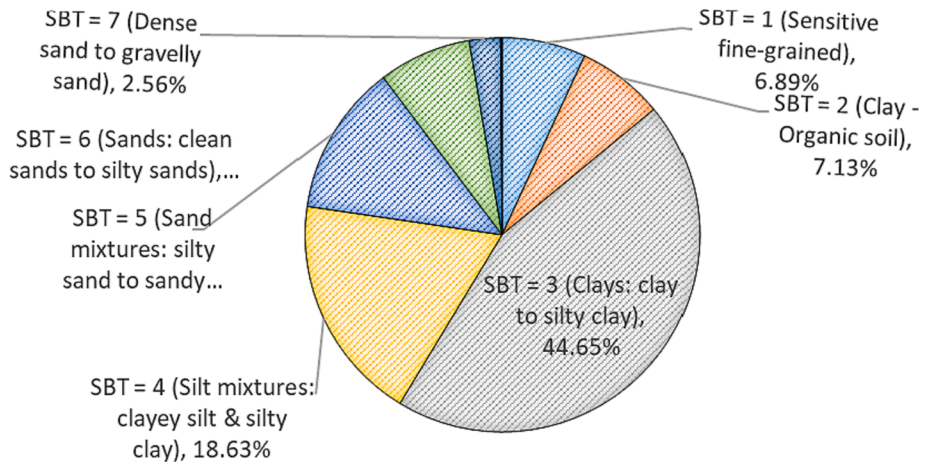


**Fig. 3.** Pi chart of soil behaviour types.

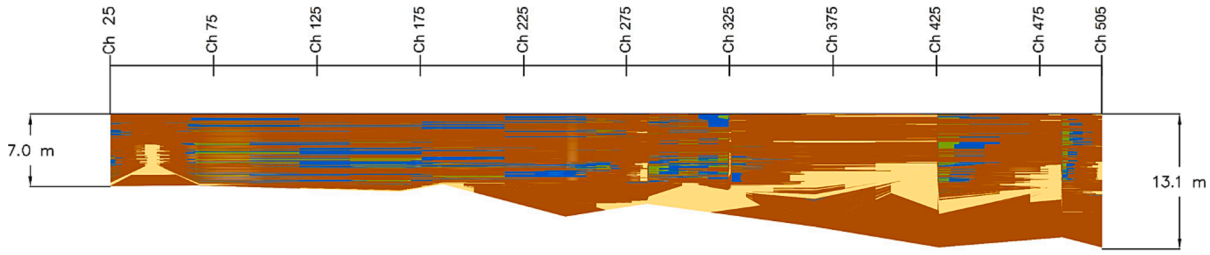


**LEGEND**

| Soil behaviour Index | Description | Colour |
|---|---|---|
| 1 | Sensitive fine-grained soils | |
| 2 | Clay – organic soils | |
| 3 & 4 | Clay & Silt mixtures (clay to silty clay) | |
| 5 and above | SANDS | |

**Fig. 4.** Long Section (along chainages) showing the different types of soil based on deterministic interpolation.

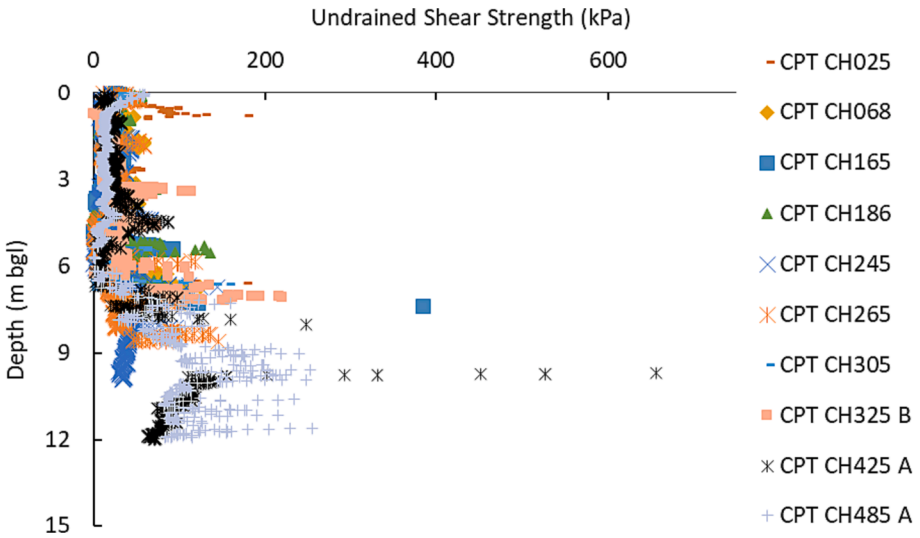


**Fig. 5.** Undrained shear strength (locations with soft clay only).

respectively. To calculate the skewness and kurtosis for log-normal distribution, $c_u$, $\mu_{c_u}$ and $\sigma_{c_u}$ in Eqs. (9) and (10) are replaced by their respective natural logarithms.

According to Eqs. (9) and (10), the normal distribution has an absolute skewness value of 2.5 and an absolute kurtosis value of 7.5. On the other hand, the log-normal distribution has an absolute skewness value of 0.1 and an absolute kurtosis value of 0.9. By definition, the distribution with the lower skewness and kurtosis is more suitable. Thereby, it is concluded that the undrained shear strength of the concerned soft clay obeys a log-normal distribution. To illustrate this conclusion, Fig. 6 shows that the surveyed undrained shear strength agrees well with the log-normal cumulative distribution with a mean shear strength$\mu_{c_u}$ = 19 kPa and a standard deviation $\sigma_{c_u}$ = 3 kPa. In contrast, the normal distribution with the calibrated arithmetic mean of 31.8 kPa and arithmetic standard deviation of 34.5 kPa does not fit the survey data.

### 3.2. Correlation length

Estimating the Correlation Length (CL), also referred to as the scale of correlation, was initially undertaken based on the deterministic method of moments (DeGroot et al., 1993). According to (Fenton et al., 2008, Vanmarcke, 2010), the CL is defined as the area under the correlation function. The correlation function is defined as:

$$\rho(r_j) = \frac{\widehat{C}(r_j)}{\widehat{C}(0)} = \frac{\widehat{C}(r_j)}{\widehat{C}(max)} \tag{11}$$

with the covariance function being

$$\widehat{C}(r_j) = \frac{1}{n}\sum_{i=1}^{n-j+1}(Y_i - m_y)(Y_{i+j-1} - m_y) \tag{12}$$

where $r_j$ is the distance in the direction of measurement; $Y_i$ is the discrete parameter in a particular direction, for instance the undrained shear strength $c_u$ in horizontal or vertical direction); and $m_y$ is the sample average of $Y_i$ in the specific direction.

The correlation function is a hypothesis (Cami et al., 2020, Fenton et al., 2008, Phoon et al., 1999) which, for soils, decays exponentially and is expressed as

$$\rho(r_j) = \frac{\widehat{C}(r_j)}{\widehat{C}(0)} = e^{-\left(\left|\frac{Ar_j}{CL}\right|\right)^B} \tag{13}$$

where $\widehat{C}(0)$ is the maximum covariance function and $A$ and $B$ are factors. Typically, $B$ is in the range of 1 to 2 (Agbaje et al., 2022, Fenton et al., 2008). Particularly, $B = 1$ indicates the Markov correlation function, whereas $B = 2$ implies the Gaussian correlation function.

#### 3.2.1. Vertical correlation length

Fig. 7 shows typical vertical correlation functions (i.e., Eqs. (11) & (12)) from the survey data where spikes are observed in the functions from CPT CH 068, CPT CH 245, CPT CH 425A, CPT CH 485A, for instance, at the depth where impurities, such as sands, exist (ISBT = 5 or greater are first encountered). To further explore the relationships between the spikes and impurities, a plot comparing the location of spikes versus the location of encountered sands in the concerned soft clay is illustrated in Fig. 8. Clearly, it is shown that the spikes occur at locations where there is a change between soft clays and sands. This also echoes the finding from (Agbaje et al., 2022) that the change from granular soils to soft clays leads to spikes.

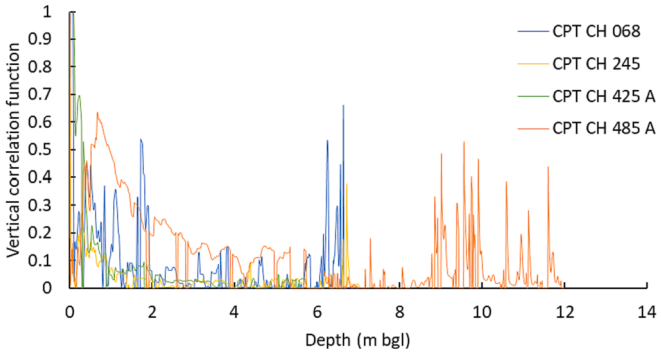


**Fig. 7.** Vertical correlation functions based on CPT survey data.

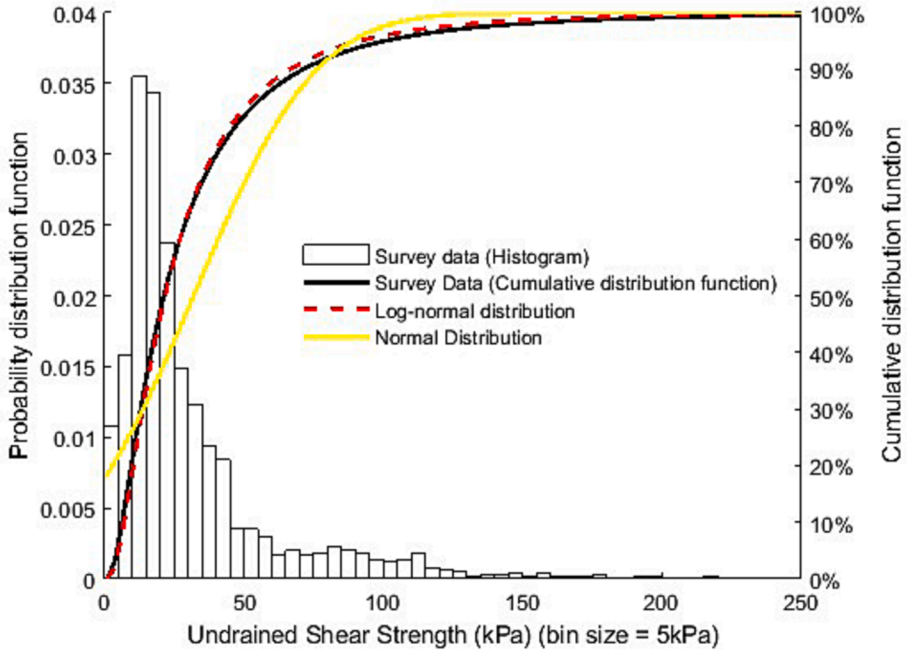


**Fig. 6.** Statistical distribution of undrained shear strength.

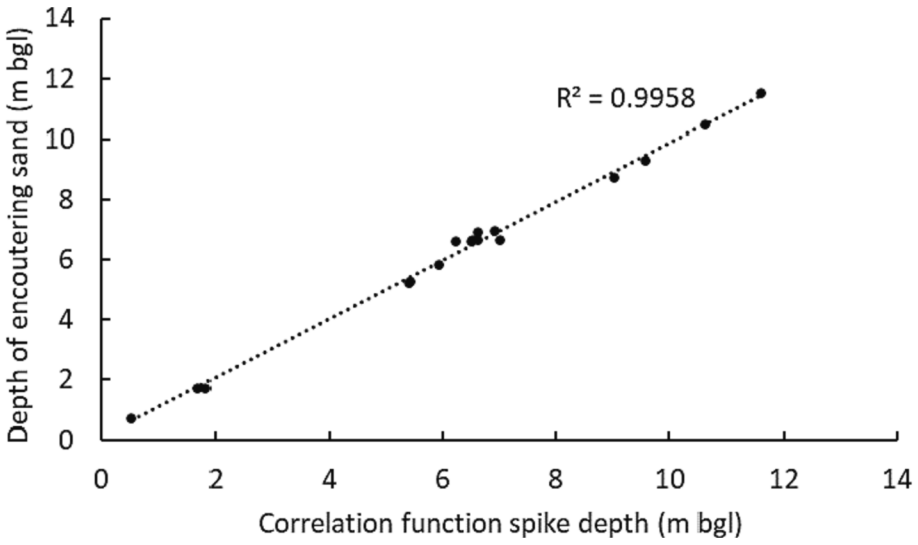


**Fig. 8.** Vertical correlation function spikes versus sand depths.

Given the existence of spikes in the correlation function and the considerable differences between the functions from different CPTs as shown in Fig. 7, Bayesian Inference (Lye et al., 2021) was employed in this study to gain possible correlation functions for the survey data (prior) so that correlation length can be calibrated. The updated correlation functions were from the algorithm TEMCMC proposed in (Lye et al., 2022) with the Markov correlation function ($B = 1$). In this study, a total of 3000 posterior correlation function curves have been generated, which were sufficient to reach a converged solution in the probabilistic limit analysis. For clarity, 200 posterior curves (in black) are illustrated in Fig. 9. As shown, all the generated curves obey the exponential function $\rho(r_j) = e^{-a_y y}$. The factor $a_y$ obeys a normal distribution function with a mean of 5 and a standard deviation of 1.66 as depicted in Fig. 10. Fig. 10 also shows a plot of $CL_y$ versus $a_y$. Since the survey data $a_y$ is less than 0.27, the maximum value of $CL_y$ from our study is 3.67. Generally, the accuracy of CPTs is limited to a minimum of 0.01 m intervals; thus, the minimum value of $CL_y$ is assumed to be 0.01 as well.

### 3.2.2. Horizontal correlation length

The horizontal correlation length ($CL_x$) was obtained using a similar approach, but with the variation of $c_u$ considered along the chainage. As this study focuses on determining the properties of soft clays, data from locations where sands exist were excluded. Specifically, only 10 CPT locations from Fig. 5 were utilised. This exclusion may result in a gap in the data for calibrating $CL_x$. Therefore, data interpolating is necessary to fill this gap. Only depths with a minimum of 3 CPT chainage points at that depth was utilised for assessing $CL_x$.

The vertical covariance function has a distinct starting point (i.e., soil/non-soil boundary at ground level). Typically, the maximum value of the covariance function occurs at ground level with the function decaying with depth. However, for the horizontal covariance, we usually do not have a starting point or soil/non-soil boundary. Thus, in this study, the starting point was taken to be the location with the largest covariance function at each depth.

The reason for this lies in the fact that the correlation function, used to derive the correlation length, is the normalised version of the covariance function. In other words, the correlation function results from dividing the covariance function by the maximum data of the covariance function as shown in (13). Consequently, the maximum value of a correlation function is always 1, and it diminishes to

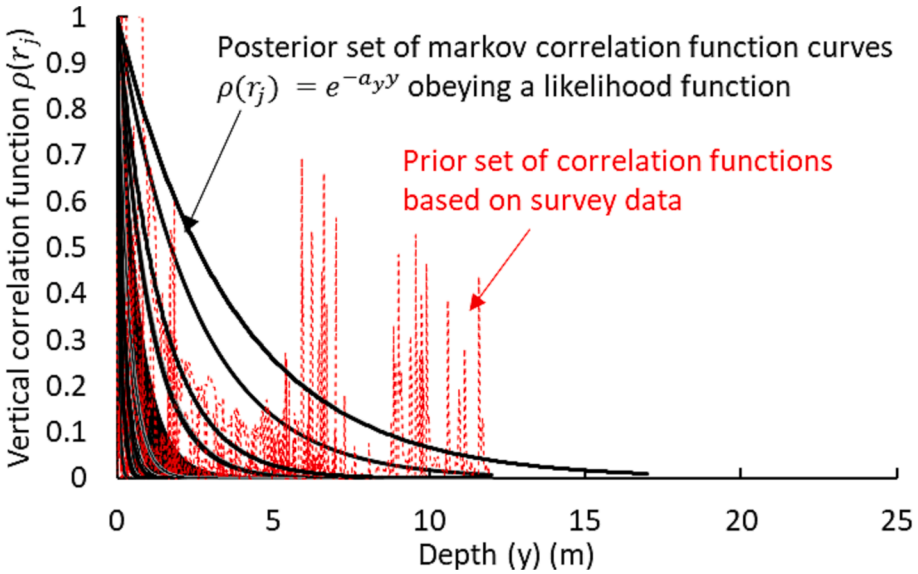


**Fig. 9.** Bayesian inference vertical correlation function curves.

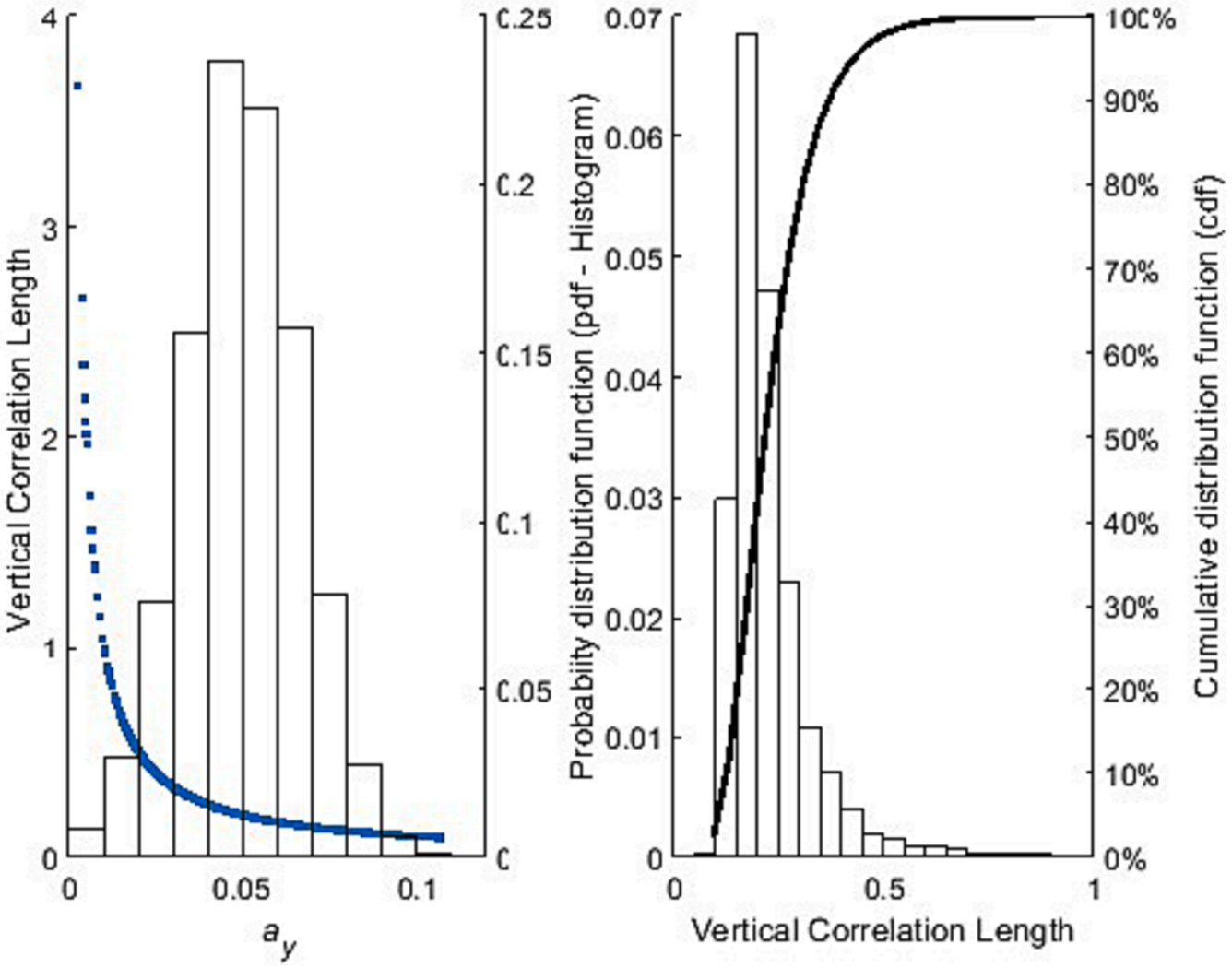


**Fig. 10.** Bayesian inference vertical correlation length ($CL_y$).

0 (typically following an exponential decay function), while the covariance function can have any numerical maximum. This conventional approach has been employed in the works of Fenton et al. (2008) and Ching et al. (2019). Therefore, by definition, for an exponentially decaying function like the Markov correlation function, which was used to model the correlation function curves (black curves as illustrated in Fig. 12), they will always initiate from the point with the maximum correlation function.

Correlation functions at different depths were consequently lag-removed. Specifically, all starting points (points with maximum auto-correlation function) have been taken as the horizontal value of 0 m with decay measured from these points. Fig. 11 shows some of the survey horizontal correlation functions with starting point lag-removed.

As per the vertical correlation length, Bayesian inference was applied to determine posterior Markov curves to fit the data for calibrating $CL_x$. The updated correlation function curves are shown in Fig. 12, which all obey an exponential function, $\rho(r_j) = e^{-a_x x}$, where $a_x$ has a normal distribution (see Fig. 13) as $a_y$ does. However, $a_x$ has a lower mean of 0.05 and a standard deviation of 0.0166. According to the Fig. 13, the maximum value of $CL_x$ for the concerned soft clay is 367 while its minimum value is 8. The minimum value is referred to the point where $a_x$ is at 3 standard deviations from the mean (0.02 % probability of occurring).

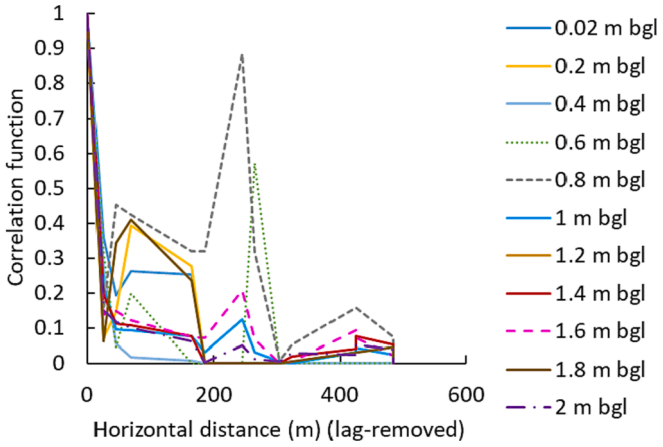


**Fig. 11.** Horizontal correlation function - survey data (11 levels from the top 2 m shown due to clarity).

## 4. Generation of random fields

A single random variable approach was employed in both the failure and post-failure analyses. It involved defining a shear strength parameter, such as cohesion, as a probability distribution function. The

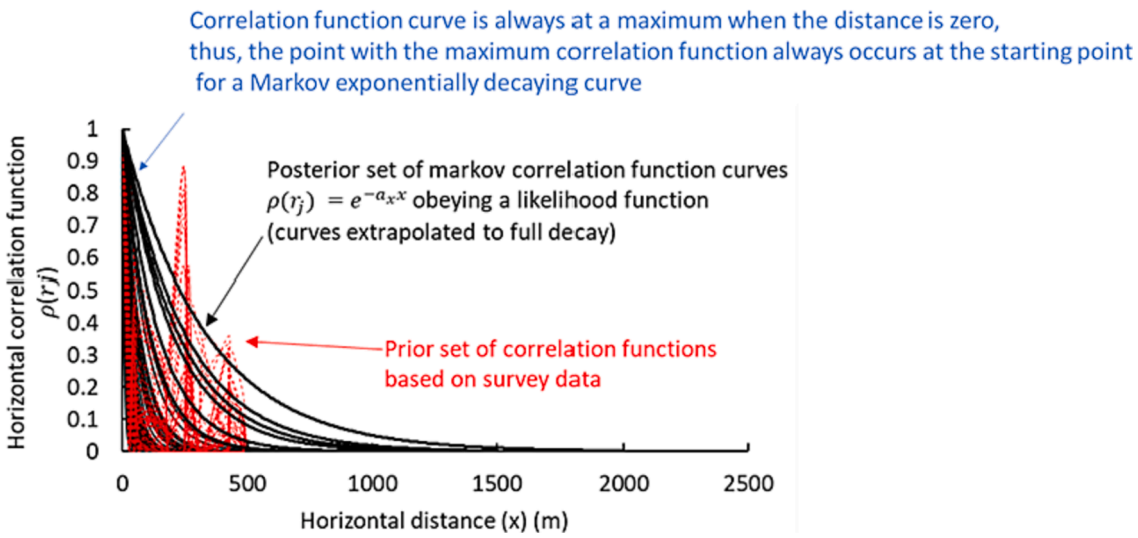


**Fig. 12.** Bayesian inference horizontal correlation function curves.

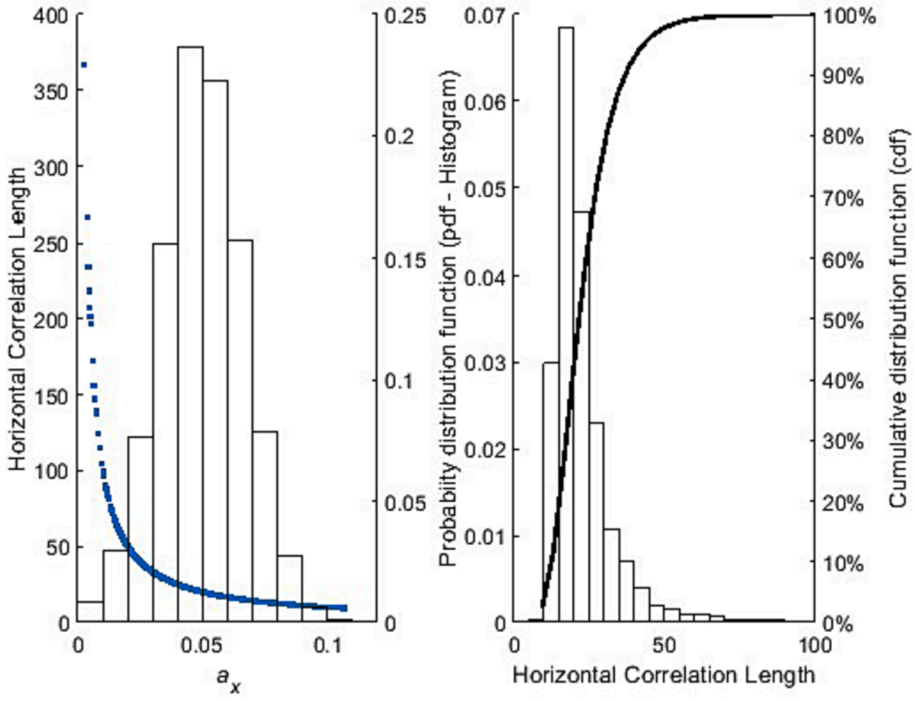


**Fig. 13.** Horizontal correlation length.

geometry of the vertical slope under investigation is shown in Fig. 14.

To generate a randomly distributed cohesion across the vertical slope shown in Fig. 14, we first generate a random field for a domain much larger than the slope geometry, followed by mapping the cohesion from the domain to the slope, as illustrated in Fig. 15. The verification of the generated random fields was also carried out through post-random field generation checks. These checks demonstrated that the input and output mean, standard deviation, and vertical correlation length values were approximately equal. This was accomplished by extracting multiple random horizontal and vertical strata of data points within the slope domain to assess the convergence of input and output values. An illustration of this process is presented for the case of a slope height of 4.47 m in Fig. 16 as a demonstration.

## 5. Results and discussions

### 5.1. Failure analyses

The mixed limit analyses were conducted to study the stability of the vertical cut slope under consideration (Fig. 14). For clay soils with a constant value of $c_u$, the critical height $H_{cr}$ at which the FoS of a slope equals 1 can be calculated using the following equation:

$$H_{cr} = N_s c_u / \gamma \tag{14}$$

where $\gamma$ is the unit weight of the soil. Although $c_u$ can vary within the range of $\pm$ 50 kPa, as indicated in our data, the variation in $\gamma$ is typically less than $\pm$ 2 kN/m$^3$ for a given soil, as shown in (BSI, 2015). In the interest of simplicity and focused research, a single uniform value of 17 kN/m$^3$ has been used to represent the unit weight of low-strength clays,

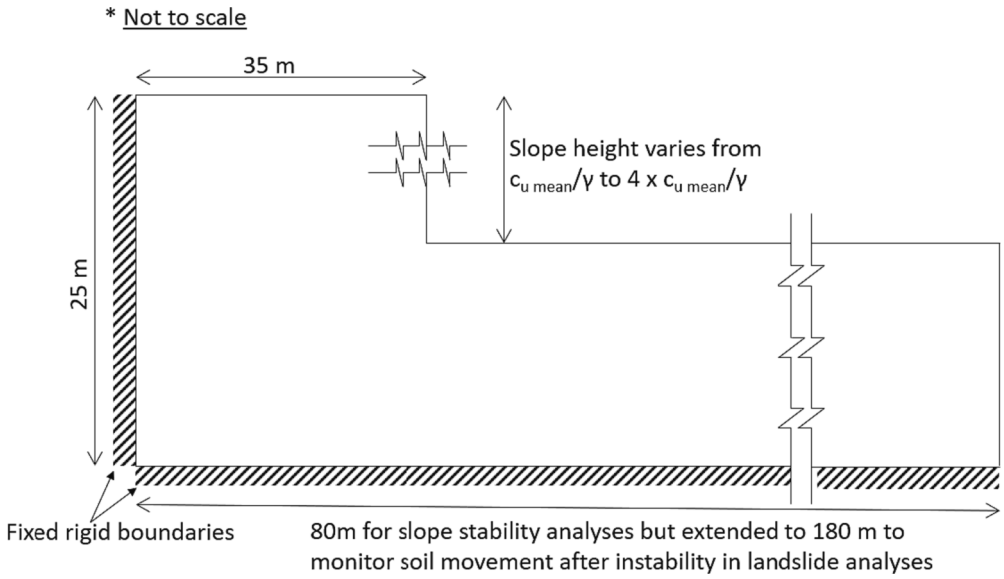


**Fig. 14.** Vertical cut geometry for slope stability and landslide analyses.

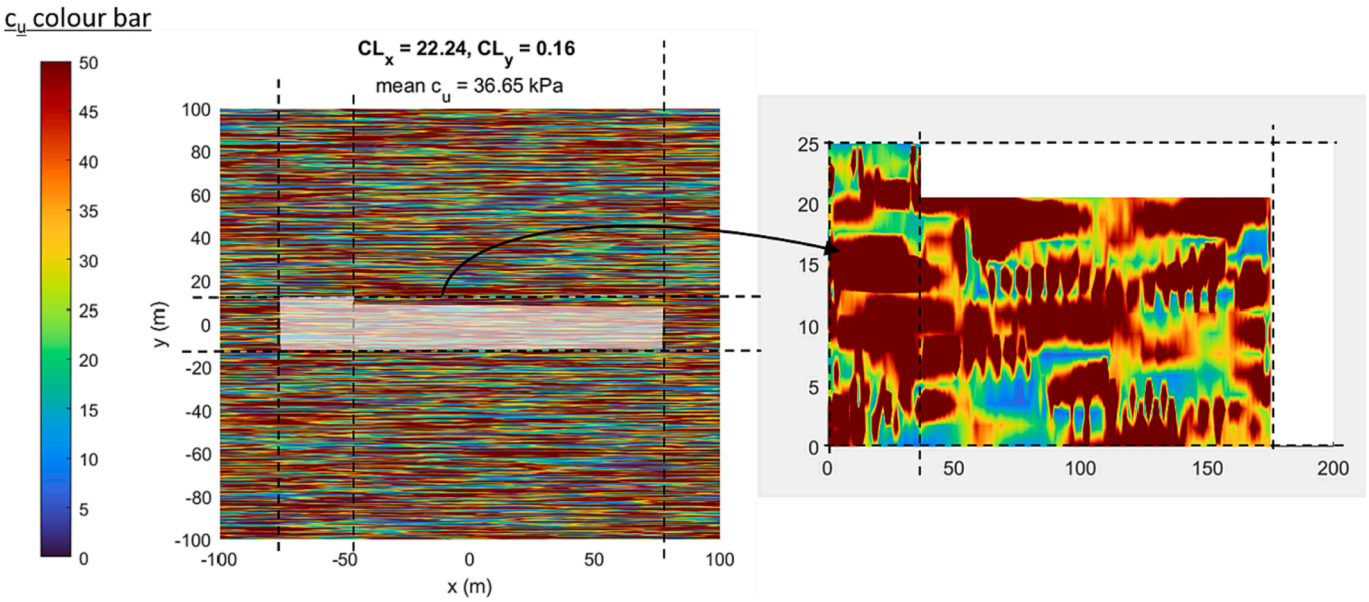


**Fig. 15.** Sample random field generation using the FFT transform and mapping onto a slope geometry for analyses.

γ, in all analyses. The semi deterministic analysis was first conducted followed by comprehensive probabilistic analyses with particular attention given to the influence of the correlation length.

*5.1.1. Semi deterministic analyses*

For slope stability analyses, a deterministic approach is characterised by the absence of spatial variability. In this study, it means that a uniform value of $c_u$ is applied throughout the entire domain or geometry. According to the UK-based industry standard Ciria R185 (Nicholson et al., 1999), choosing a single uniform value typically corresponds to the most probable value, often associated with a likelihood of occurrence of 1 in 2 or the 50th percentile probability. Alternatively, when applying a partial factor of safety, the preference is generally for a value from the conservative side of the distribution curve of soil strength results. However, an important question arises: 'How far into the safer side of the distribution curve is considered safe enough?' In other words, what is the optimal value of the partial factor to account for the variability of $c_u$? For the Eurocode 7 design standard (EN, 1997-1), a partial factor of 1.4 is applied to $c_u$. Nonetheless, BS EN 1990 (EN, 2002) clause 3.5 (5) in the Eurocode also suggests an alternative approach to the partial factor method, wherein a design directly based on probabilistic methods can be employed. Therefore, in this section, the Probability of Failure (PoF) was initially computed using a semi-deterministic approach.

In the semi-deterministic approach, instead of selecting a single value of $c_u$ as performed in deterministic analyses, a series of analyses are undertaken using multiple values that correspond to different percentages derived from the Cumulative Distribution Function (CDF). For instance, Fig. 17 illustrates that an analysis employing a $c_u$ value of 19 kPa corresponds to a CDF of 50 %, while a $c_u$ value of 9 kPa corresponds to a CDF of 20 %, and so on. The CDF represents the cumulative probability of observing a soil strength at the site based on the collected data. Fig. 18 presents a semi-deterministic parametric study of the FoS achieved at various slope heights for $c_u$ values representing different CDF

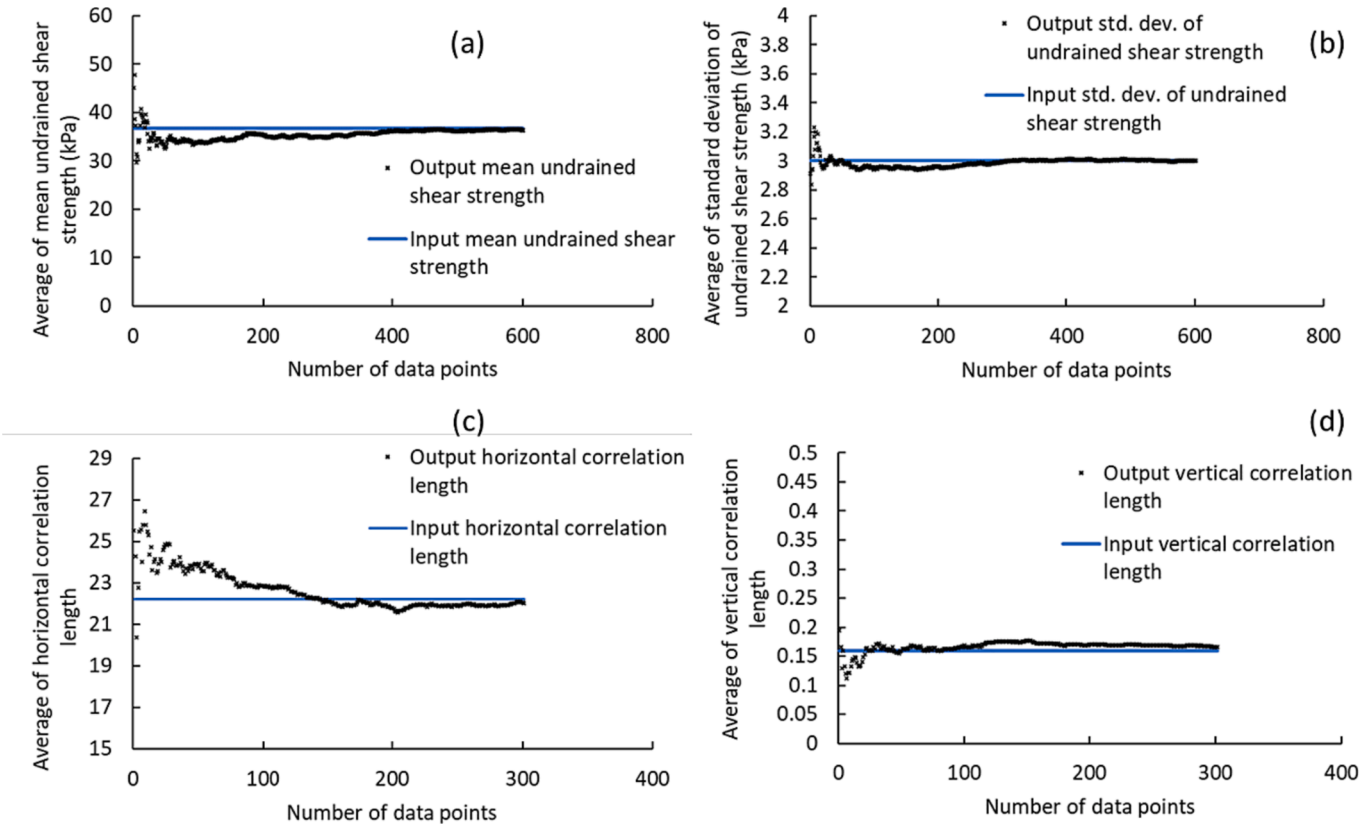


**Fig. 16.** Verification of generated random field.

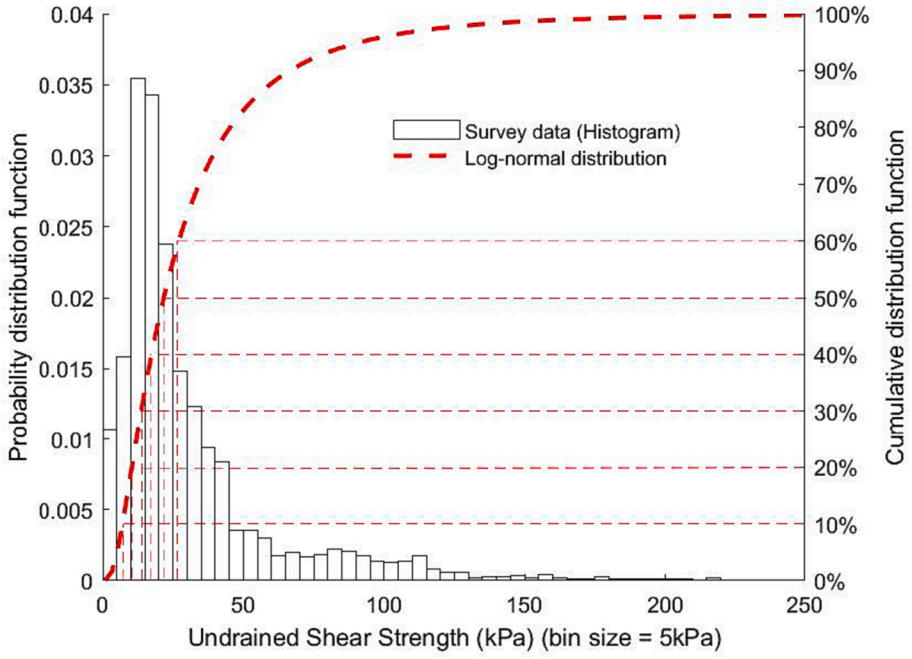


**Fig. 17.** Semi-deterministic CDF.

percentages derived from the data pertaining to low-strength soils. In the semi-deterministic analyses, the PoF corresponds to the likelihood of observing the $c_u$ value for a specific slope stability height where the Factor of Safety (FoS) is less than 1. In other words, it is the cumulative distribution function (CDF) percentage derived from the site data (refer to Fig. 17) when the FoS equals 1.0 for a given slope (as shown in Fig. 18). The results from Fig. 18 will be subsequently utilised later for comparison with the findings obtained from the probabilistic analyses.

### 5.1.2. *Probabilistic analyses*

The comprehensive probabilistic analyses were subsequently conducted to calculate the FoS of the vertical slope by incorporating spatial

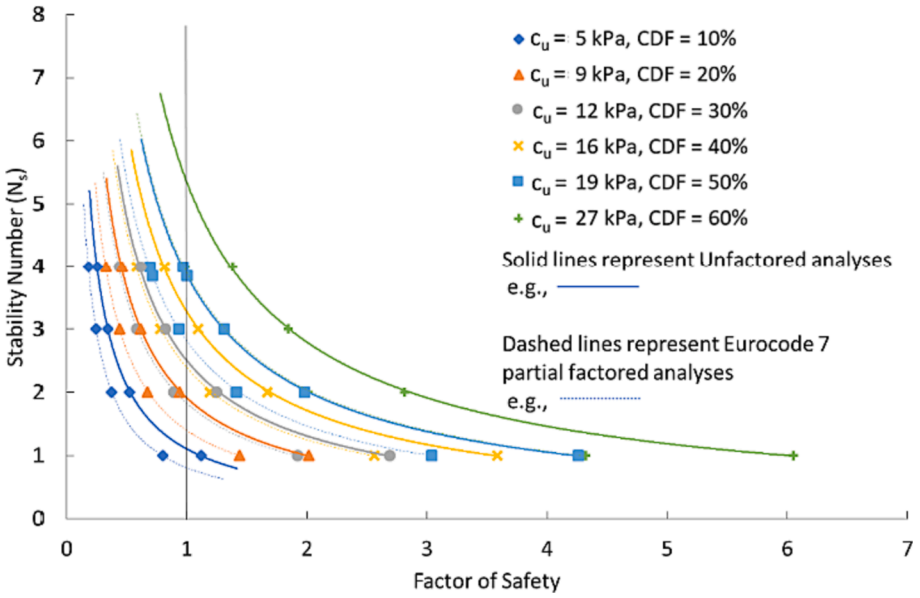


**Fig. 18.** Semi-deterministic analyses - Factors of Safety.

variability, as opposed to the non-spatial variability considered in the deterministic/semi-deterministic analyses. These analyses were performed as part of a parametric study, where the vertical cut height was varied with $N_s$ ranging from 1 to 4. A series of Monte Carlo simulations were executed with the mixed limit analyses and generated random fields to determine the FoS. An illustrative plot, shown in Fig. 19, depicts the case of $N_s = 2$. It demonstrates that by considering the probabilistic $c_u$, as well as the probabilistic $CL_x$ and $CL_y$ (Fig. 10 and Fig. 12) to generate the random fields, the mean FoS of the series tends to converge after approximately 3000 random simulations. Similar trends were observed across cases where $N_s$ ranged from 1 to 4, indicating that 3000 Monte Carlo simulations proved sufficient for the analyses.

By definition, the PoF represents the percentage of unstable slope stability analyses among all probable slope stability analyses. For the probabilistic analyses in this study, the PoF is simply calculated as the ratio of the number of unstable slopes to the total number of slopes obtained from the Monte Carlo simulations. A convergence analysis was conducted to examine the influence of mesh size on the PoF. Initially, a series of analyses were performed by varying the mesh size and calculating the PoF. Fig. 20 illustrates the results for the case where $H_{cr}$ ranges from $c_u/\gamma$ to $4c_u/\gamma$. In all the probabilistic analyses, the log-normal mean (19 kPa) was considered a more suitable measure of central tendency than the arithmetic mean (31.8 kPa), due to the log-normal distribution of the data explained in Section 3.1. The analyses presented in Fig. 20 represent a set of simulations where the correlation lengths were allowed to vary based on the probability distribution depicted in Fig. 10 and Fig. 13. The results demonstrated that the accuracy of the PoF was affected by the mesh density up to a density of 13.3 nodes per $m^2$. For instance, as depicted in Fig. 20, when considering the case of$H_{cr} = 4c_u/\gamma$, the PoF increases from 47% (at 0.9 nodes per $m^2$) to 54% (at 13.3 nodes per $m^2$) with an increase in mesh density. Beyond this point, a converged PoF is achieved. If not otherwise specified, the presented results for all probabilistic analyses were obtained using a mesh density of 13.3 nodes per $m^2$.

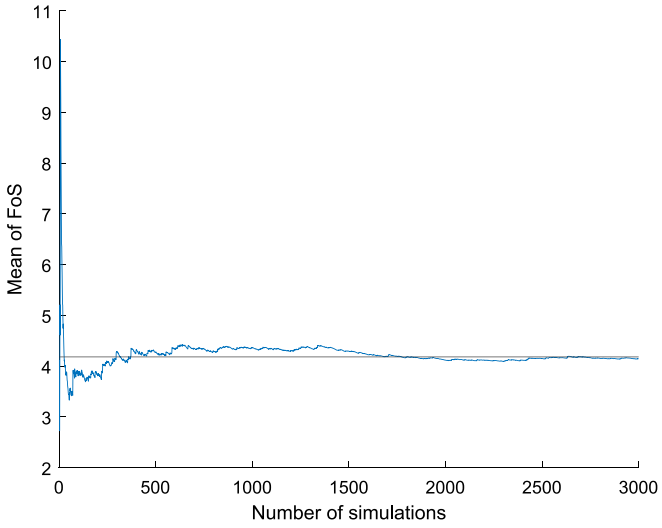


**Fig. 19.** Probabilistic analyses calibration of number of Monte Carlo simulations required.

### 5.1.3. *Comparison and discussion*

Fig. 21 displays a comparison between the PoF obtained from the semi-deterministic and probabilistic analyses. Two sets of probabilistic analyses were illustrated: one incorporating Monte Carlo sampling of correlation lengths from the distributions depicted in Fig. 10 and Fig. 13, and another where only the median values of the correlation length were sampled from both figures. By juxtaposing the unfactored semi-deterministic results (without considering the correlation length) with the probabilistic results (considering the correlation length), it becomes evident that the PoF values obtained from the semi-deterministic analyses, and both sets of probabilistic analyses are highly similar.

These results are intriguing as they demonstrate that calculating the PoF using a non-spatially variable analysis with an accurate semi-deterministic approach yields equivalent results to a Monte Carlo random field analysis with spatial variability. Furthermore, the findings indicate that performing a full probabilistic analysis by varying the correlation lengths according to the distribution curves from Fig. 10 and Fig. 13 only provides a marginal improvement of 0% to 2% compared to probabilistic analyses where only the median correlation lengths derived from Bayesian Inference were utilized.

Remarkably, the computational demands of the semi-deterministic analysis are substantially lower compared to those of a comprehensive probabilistic analysis, primarily due to the requirement of a significantly larger number of simulations in probabilistic analyses. For instance, in this case, the probabilistic analyses entailed 3000 Monte Carlo

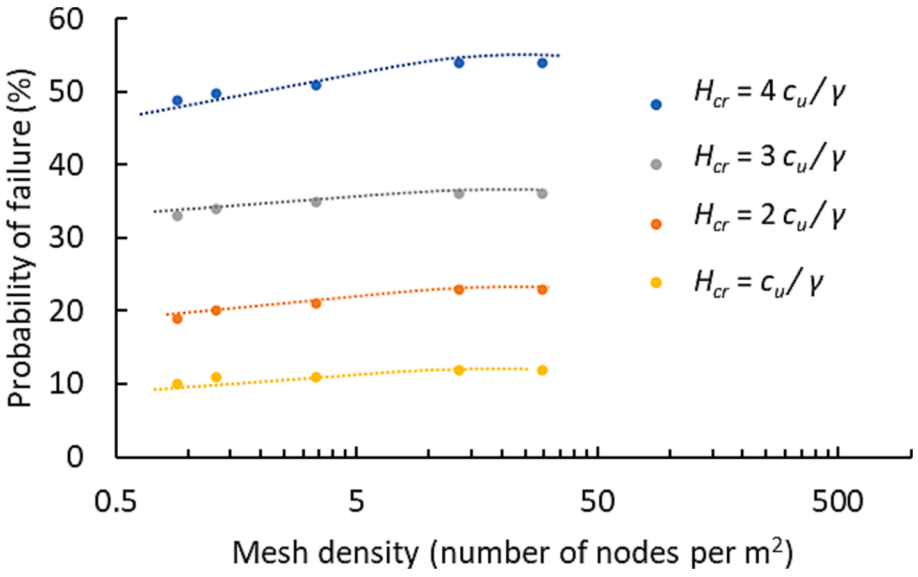


**Fig. 20.** Mesh density vs probability of failure.

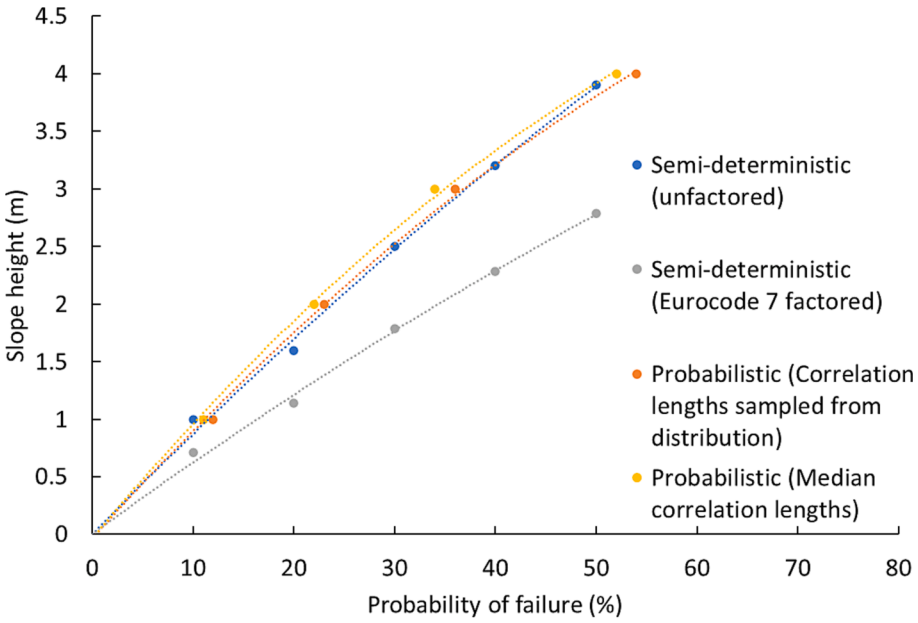


**Fig. 21.** Probability of failure (mesh density = 13.3 nodes/m$^2$).

simulations for a single slope geometry, whereas only 6 analyses per slope geometry were performed for the semi-deterministic analyses.

### 5.2. Post-failure analyses

In this section, cases with FoS less than 1 were re-analysed using the N-PFEM to investigate their post-failure stages. Fig. 22 presents an example of the visualisation of three distinct failure mechanisms observed in the slope stability analyses ($N_s$ = 4) derived from the probabilistic analyses. These mechanisms are referred to as Stage 1 of the analyses, representing the initial state where no movement has occurred. Subsequent stages pertain to landslide analyses where further movement takes place.

The visualisations reveal that, in all three cases, the primary factor contributing to instability is the presence of a low-strength layer near or just below the toe of the vertical cut. This layer exhibits high plastic strains. A rotational slip surface has been super-imposed on the slopes, denoting a similar failure surface as expected in deterministic analysis. However, the key distinction in the probabilistic failure surfaces is the occurrence of multiple fuzzy bands of plastic strains within the zone bounded by the rotational surface and the vertical cut. For instance, in Fig. 22(c) and (d), which represent the results from the 15th case (out of 3000 Monte Carlo runs) involving a very low strength clay, the fuzzy bands of plastic strain within the rotational slip surface are more prominent, corresponding to layers of exceptionally low strength. These plastic strain bands are less prominent in simulations with higher shear strengths, as observed in Run 82 (Fig. 22(e) and (f)), where only a localised spot of plastic straining occurs at the toe.

For the post-failure analyses, the simulations were continued until the maximum velocity within all nodes in the analysis domain dropped below 0.00001 m/s. To maintain conciseness, landslides extending beyond 125 m from the front of the slope were excluded, as they represent cases where the soil exhibits high flow and fluid-like properties for the geometry of the cutting vertical slope in consideration.

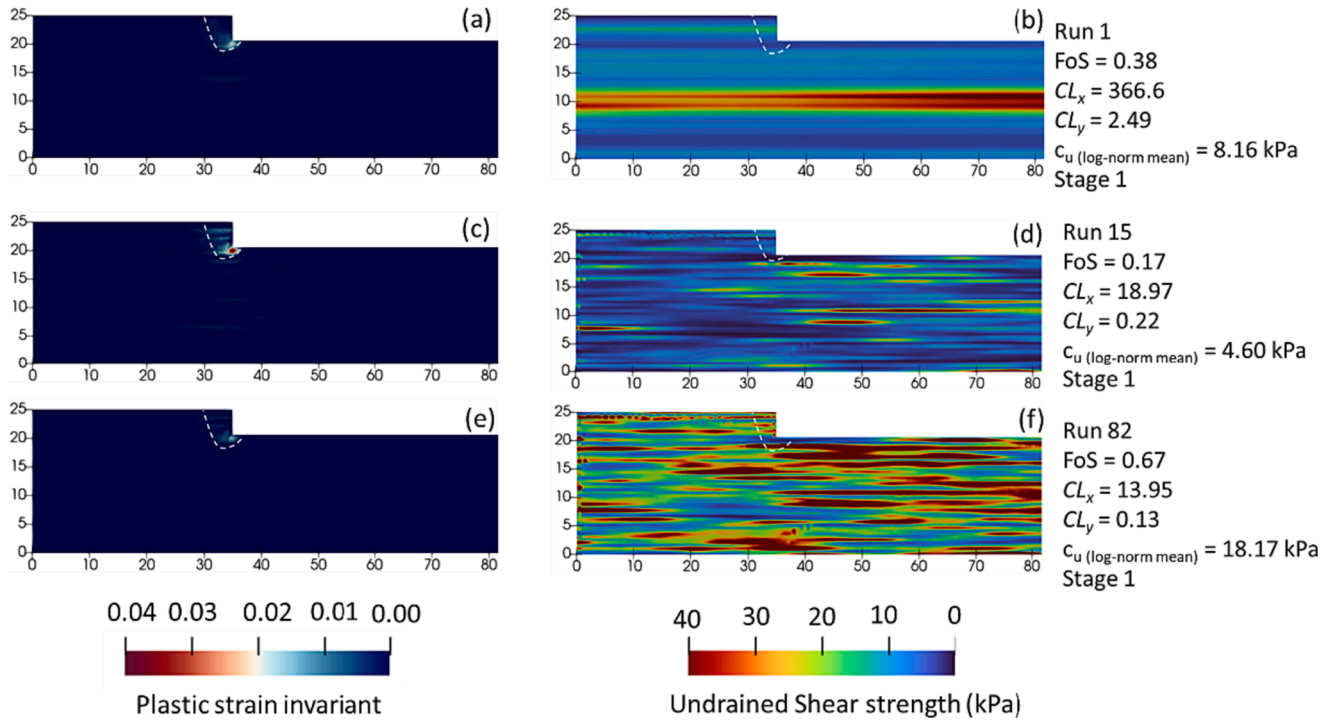


**Fig. 22.** Failure mechanism for various typical analyses.

Additionally, a landslide was deemed to have reached a final runout distance if an increase in ground level of 125 mm occurred at that distance due to the landslide. This threshold of 100 mm was selected which is slightly smaller than the height of a standard motorway kerb (i.e., 125 mm).

Fig. 23 illustrates the progression of a typical post-failure landslide obtained from the N-PFEM simulation. Starting from an initial stage (i.e., stage 0 as shown in Fig. 23(a)) where no movement or failure is observed, the plastic strain bands gradually develop and migrate, becoming more prominent. The landslide exhibits both forward movement and retrogressive slip surfaces, leading to soil loss and instability in the opposite direction of the landslide flow. In Fig. 23(k), multiple quasi-rotational slip surfaces can be observed, indicating a complex pattern of fuzzy failure has occurred. These intricate fuzzy failure bands can be attributed to the spatial variability and horizontal layering induced by the random fields.

The velocity of a landslide is a crucial factor in assessing the level of risk it poses to people, infrastructure, and the environment. A faster-moving landslide can result in more destructive consequences than a slower one. Understanding the velocity is essential for evaluating potential impacts and developing appropriate mitigation measures. For slow-moving landslides, engineers may consider stabilising the slope with measures such as retaining walls or drainage systems. In contrast, rapidly moving landslides may necessitate evacuation plans and more robust engineering solutions. Fig. 24 presents the horizontal velocity of the front of the landslide at the same level of 100 mm above ground level for Run 18 (Fig. 23). This depiction reveals that the landslide velocity profile follows a parabolic trend. This parabolic velocity behaviour agrees well with the findings of Pudasaini et al. (2022) who also reported a parabolic trend of landslide velocity based on a class of nonlinear advective–dissipative system. The parabolic trend is also consistent with the classic inviscid Burgers' equation, typically used to model landslide velocities (Ma et al., 2023, Oberender et al., 2016). For the specific example with a log-norm mean $c_u$ of 5.976 kPa, a deterministic approach predicts a runout greater than 125 m, suggesting the landslide would behave in a pseudo-fluid manner. This implies that considering spatial variability does indeed provide some resistance to landslide runout.

A comparison was conducted between the results of probabilistic analysis and semi-deterministic analysis of the post-failure stages. Generally, design standards do not specify partial factors for $c_u$ when assessing movements of landslides. Therefore, a Eurocode 7 analysis in this section refers to an unfactored analysis.

For semi-deterministic analyses, where soil strength is uniform, a specific value of $c_u$ will consistently result in a particular runout distance. For instance, as depicted in Fig. 25, a semi-deterministic $c_u$ of 9 kPa and 12 kPa will always yield runout distances of 80 m and 40 m, respectively, for a slope height of 4.47 m. In contrast, probabilistic analyses predict a range of possible runout distances spanning from 0 m to over 125 m. However, 89% of these runout distances were less than 80 m and 82% were less than 40 m. In probabilistic analyses, although the vertical cut is unstable, the influence of the correlation length (spatial variability) suggests that random layers with higher soil strength have a minimal mitigating effect on reducing landslide runout. As anticipated, runout distances are directly influenced by the slope height. For instance, at a slope height of 4.47 m, 1.6% of simulations exhibited runout distances greater than 80 m, while 0.27% of simulations surpassed 80 m for a lower slope height of 1.12 m. Additionally, for a slope height of 1.12 m, 0.4% of simulations, even though unstable, had a runout distance of less than 1 m, whereas for a slope height of 4.47 m, 1.8% of simulations, even though unstable, had a runout distance of less than 1 m.

A final analysis was conducted to elucidate the pivotal parameters influencing the runout distance. This involved plotting the mean $c_u$, horizontal correlation length, and vertical correlation length against the runout distance, as depicted in Fig. 26. The results indicated that, when scrutinised individually, correlation lengths exhibited no discernible impact on the runout distance. However, drawing insights from the failure mechanism shown in Fig. 22 - where failure is contingent on plastic failure occurring at the toe of the slope, and since the occurrence of plastic failure is contingent on spatial variability - it can be deduced that the combined effect of both correlation lengths and the random field generation dictates the likelihood of a random weak spot materialising at the toe of the slope. Consequently, this combined influence

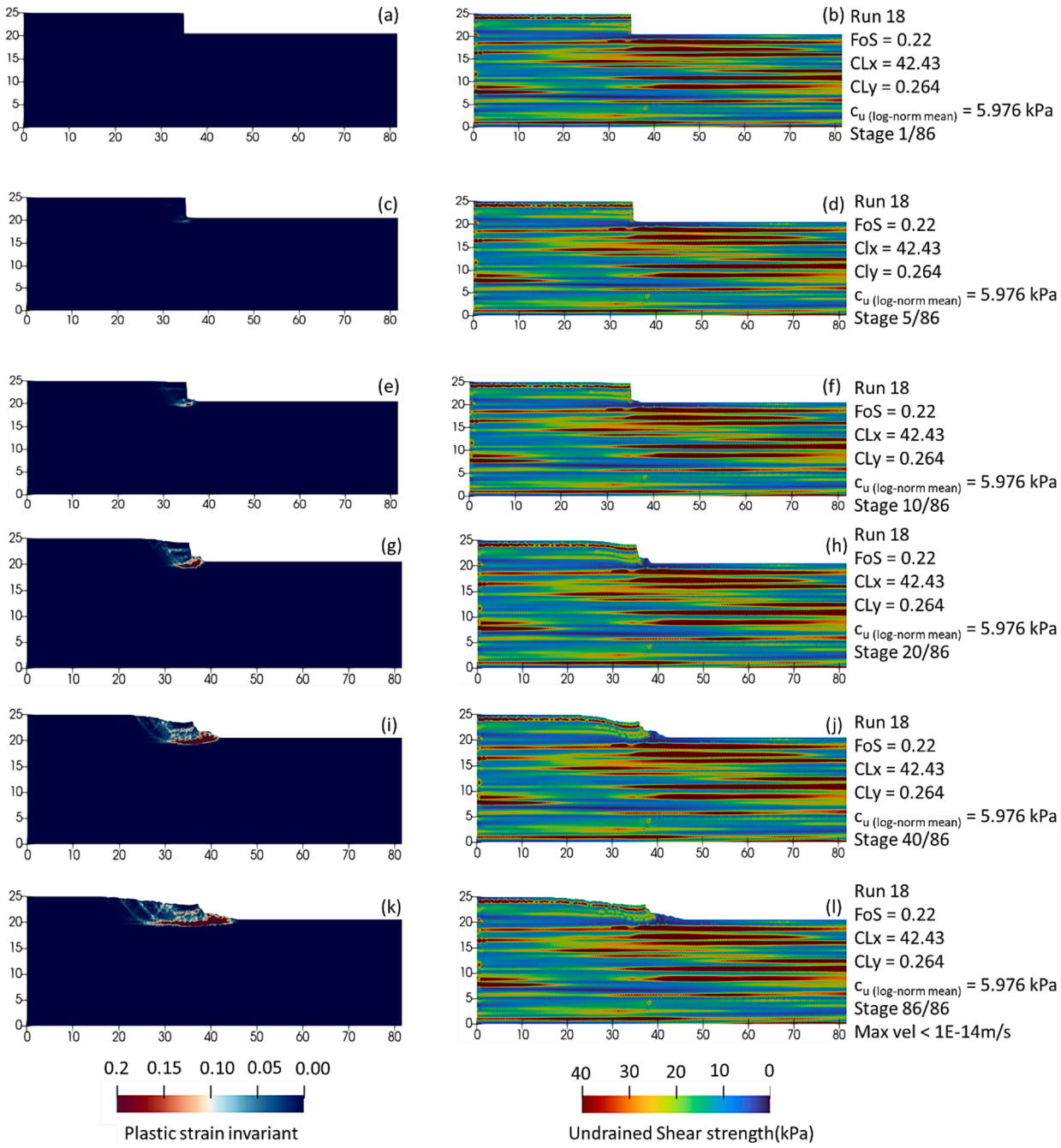


**Fig. 23.** Visualisation of post failure process from N-PFEM simulation.

bears significance in determining the runout distance. On the other hand, Fig. 26 reveals a trend with uncertainty for probabilistic runout distances concerning the mean undrained shear strength of the soil. Specifically, for landslide runout distances, the mean undrained shear strength, especially around the toe, emerges as the most significant factor. Additionally, Fig. 25 illustrates that in some cases, even with a very low mean undrained shear strength, no runout was achieved. This phenomenon is attributed to spatial variability providing some soil strength at the toe.

## 6. Conclusions

This paper presents a comprehensive investigation into the spatial variation of strength, specifically cohesion, in soft clay and its impact on slope stability analysis and post-failure analysis. In-situ cone penetration tests (CPTs) were conducted near the Tay River in Perth, Scotland, where alluvial soft clays are prevalent. The collected data was analysed to calibrate the probabilistic strength properties of the soft clays, including the distribution characteristics of undrained shear strength, vertical and horizontal correlation lengths, and more. Subsequently, slope stability analyses were performed using a mixed limit analysis to calculate the Factor of Safety (FoS) based on deterministic, semi-deterministic, and comprehensive probabilistic approaches. Additionally, in the event of slope failure, post-failure analyses were conducted using a novel continuum approach called N-PFEM to analyse the failure evolution process and final runout distance. The major findings from this research can be summarised as follows.

The surveyed undrained shear strength obeys well the log-normal cumulative distribution with a mean shear strength of 19 kPa, and a standard deviation of 3 kPa. A change between soft clays and sands

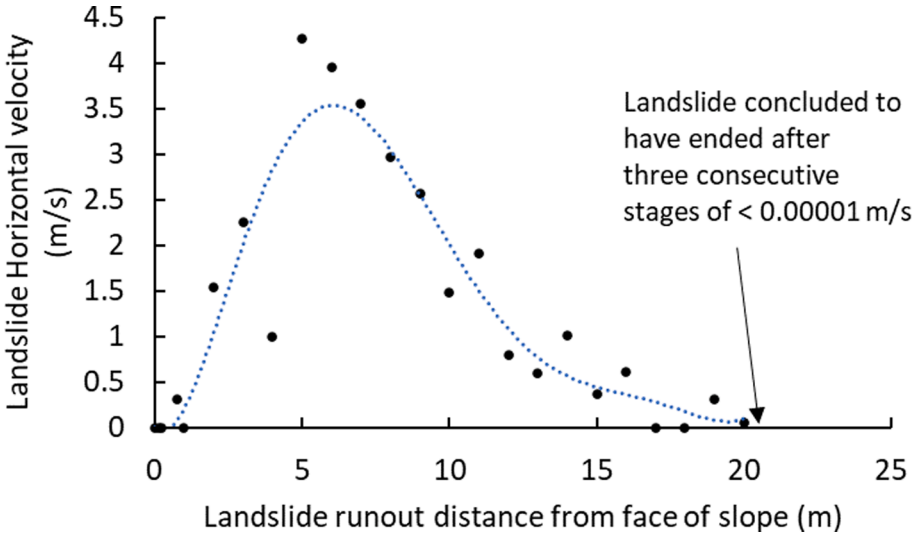


**Fig. 24.** Landslide horizontal velocity vs runout distance.

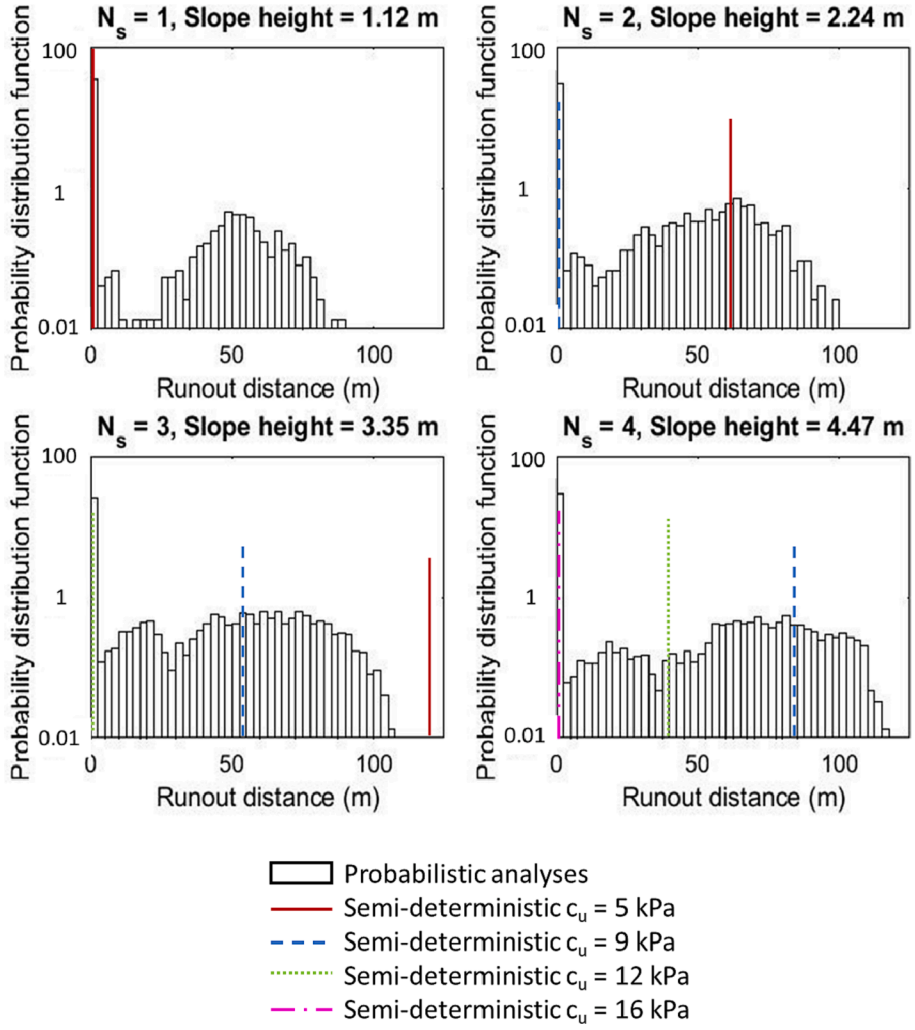


**Fig. 25.** Landslide runout distances (probabilistic vs deterministic).

results in spikes in correlation function, leading to difficulties in determining correlation length. The correlation lengths exhibit statistical distribution patterns that can be modelled using Bayesian inference. However, in the case of the investigated soft soils, treating the correlation lengths as distributions yielded only a minimal 2 % difference compared to using single centralized correlation length value such as the

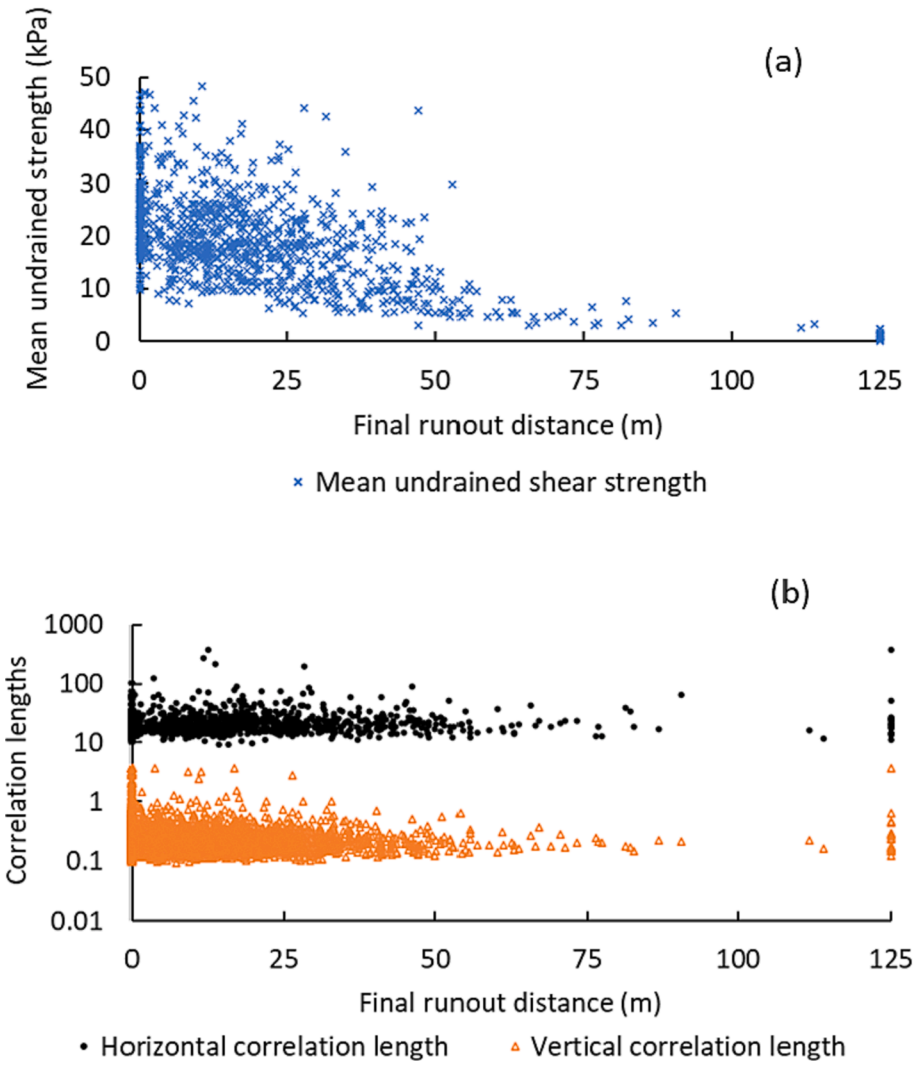


**Fig. 26.** Runout distance versus mean undrained shear strengths and correlation lengths.

median value. This is considered true for soft soils with horizontal layering similar to those in the data studied. However, further investigations are needed for soils with different correlation length characteristics, such as soils with substantial mixing rather than layering.

The semi-deterministic analyses demonstrated remarkably similar results to the probabilistic analyses in calculating the probability of failure. This provides a significant advantage over probabilistic analyses, as it significantly reduces computation time and memory requirements. Nevertheless, for post-failure analyses, the probabilistic approach provided more comprehensive results by considering the spatial variability of soils. It provided a range of runout distances with associated probabilities, whereas semi-deterministic analyses tended to yield fixed runout distances as single values.

## CRediT authorship contribution statement

**Samzu Agbaje:** Conceptualization, Methodology, Software, Visualization, Writing – original draft. **Xue Zhang:** Conceptualization, Funding acquisition, Methodology, Software, Supervision, Writing – review & editing. **Edoardo Patelli:** Conceptualization, Supervision. **Darren Ward:** Data curation. **Luisa Dhimitri:** Data curation.

## Declaration of competing interest

The authors declare the following financial interests/personal relationships which may be considered as potential competing interests: Xue Zhang reports financial support was provided by UK Research and Innovation (EP/V012169/1).

## Data availability

Data will be made available on request.

## Appendix A. Supplementary material

Supplementary data to this article can be found online at https://doi.org/10.1016/j.compgeo.2023.106037.

## References

Agbaje, S., Zhang, X., Ward, D., Dhimitri, L., Patelli, E., 2022. Spatial variability characteristics of the effective friction angle of Crag deposits and its effects on slope stability. Comput. Geotech. 141, 104532.

BSI, 2015. BS 8002: 2015. Code of practice for earth retaining structures, BSI London, UK.

Cami, B., Javankhoshdel, S., Phoon, K.-K., Ching, J., 2020. Scale of fluctuation for spatially varying soils: estimation methods and values. ASCE-ASME J. Risk Uncertainty Eng. Syst. Part A: Civ. Eng. 6 (4), 03120002.

Chen, X., Li, D., Tang, X., Liu, Y., 2021. A three-dimensional large-deformation random finite-element study of landslide runout considering spatially varying soil. Landslides 18 (9), 3149–3162.

Ching, J., Phoon, K.-K., 2019. Impact of Autocorrelation Function Model on theProbability of Failure. J. Eng. Mech. 145 (1), 04018123.

Ching, J., Wang, J.-S., 2016. Application of the transitional Markov chain Monte Carlo algorithm to probabilistic site characterization. Eng. Geol. 203, 151–167.
DeGroot, D.J., Baecher, G.B., 1993. Estimating autocovariance of in-situ soil properties. J. Geotech. Eng. 119 (1), 147–166.
Dyson, A.P., Tolooiyan, A., 2019. Prediction and classification for finite element slope stability analysis by random field comparison. Comput. Geotech. 109, 117–129.
EN, B., 1997-1. Eurocode 7: Geotechnical design-part 1: General rules. British Standards, UK.
EN, B., 2002. Eurocode—Basis of structural design, Brussels.
Fenton, G.A., Griffiths, D.V., 2008. Risk assessment in geotechnical engineering. John Wiley & Sons New York.
Griffiths, D., Fenton, G.A., 1997. Three-dimensional seepage through spatially random soil. J. Geotech. Geoenviron. Eng. 123 (2), 153–160.
Jiang, S.-H., Huang, J., Huang, F., Yang, J., Yao, C., Zhou, C.-B., 2018. Modelling of spatial variability of soil undrained shear strength by conditional random fields for slope reliability analysis. App. Math. Model. 63, 374–389.
Krabbenhøft, K., Lyamin, A.V., Sloan, S.W., 2007. Formulation and solution of some plasticity problems as conic programs. Int. J. Solids Struct. 44 (5), 1533–1549.
Li, J., Tian, Y., Cassidy, M.J., 2015. Failure mechanism and bearing capacity of footings buried at various depths in spatially random soil. J. Geotech. Geoenviron. Eng. 141 (2), 04014099.
Liu, X., Wang, Y., 2021. Probabilistic simulation of entire process of rainfall-induced landslides using random finite element and material point methods with hydro-mechanical coupling. Comput. Geotech. 132, 103989.
Lunne, T., Powell, J.J., Robertson, P.K., 2002. Cone penetration testing in geotechnical practice. CRC Press.
Lye, A., Cicirello, A., Patelli, E., 2021. Sampling methods for solving Bayesian model updating problems: A tutorial. Mech. Syst. Sig. Process. 159, 107760.
Lye, A., Cicirello, A., Patelli, E., 2022. An efficient and robust sampler for Bayesian inference: Transitional ensemble Markov chain Monte Carlo. Mech. Syst. Sig. Process. 167, 108471.
Ma, G., Rezania, M., Nezhad, M.M., 2022. Stochastic assessment of landslide influence zone by material point method and generalized geotechnical random field theory. Int. J. Geomech. 22 (4), 04022002.
Ma, L., Zhao, L., Wang, X., 2023. An iteration-free semi-Lagrangian meshless method for Burgers' equations. Eng. Anal. Bound. Elem. 150, 482–491.
Meng, J., Zhang, X., Huang, J., Tang, H., Mattsson, H., Laue, J., 2020. A smoothed finite element method using second-order cone programming. Comput. Geotech. 123, 103547.
Meng, J., Zhang, X., Utili, S., Oñate, E., 2021. A nodal-integration based particle finite element method (N-PFEM) to model cliff recession. Geomorphology 381, 107666.
Nguyen, H.C., 2023. A mixed formulation of limit analysis for seismic slope stability. Géotech. Lett. 13 (1), 54–64.
D. Nicholson, C.-M. Tse, C. Penny, S. O Hana and R. Dimmock, 1999. The observational method in ground engineering: principles and applications. Report - Construction industry research and information association **185**.
Oberender, P.W., Puzrin, A.M., 2016. Observation-guided constitutive modelling for creeping landslides. Geotechnique 66 (3), 232–247.
Phoon, K.-K., Kulhawy, F.H., 1999. Characterization of geotechnical variability. Can. Geotech. J. 36 (4), 612–624.
Pudasaini, S.P., Krautblatter, M., 2022. The landslide velocity. Earth Surf. Dyn. 10 (2), 165–189.
Robertson, P., Campanella, R., 1983a. Interpretation of cone penetration tests. Part II: Clay. Can. Geotech. J. 20 (4), 734–745.
Robertson, P.K., Campanella, R., 1983b. Interpretation of cone penetration tests. Part I: Sand. Can. Geotech. J. 20 (4), 718–733.
Selmi, M., Kormi, T., Hentati, A., Ali, N.B.H., 2019. Capacity assessment of offshore skirted foundations under HM combined loading using RFEM. Comput. Geotech. 114, 103148.
Tan, X., Wang, X., Khoshnevisan, S., Hou, X., Zha, F., 2017. Seepage analysis of earth dams considering spatial variability of hydraulic parameters. Eng. Geol. 228, 260–269.
Vanmarcke, E., 2010. Random fields: analysis and synthesis. World Scientific.
Yi, J.T., Pan, Y.T., Huang, L.Y., Xu, S.J., Liu, Y., Phoon, K.K., 2020. Determination of limiting cavity depths for offshore spudcan foundations in a spatially varying seabed. Mar. Struct. 71, 102723.
Zhang, X., Oñate, E., Torres, S.A.G., Bleyer, J., Krabbenhoft, K., 2019. A unified Lagrangian formulation for solid and fluid dynamics and its possibility for modelling submarine landslides and their consequences. Comput. Methods Appl. Mech. Eng. 343, 314–338.
Zhang, X., Meng, J., Yuan, S., 2022. An implicit nodal integration based PFEM for soil flow problems. Comput. Geotech. 142, 104571.
Zhang, Y., Zhang, X., Nguyen, H., Li, X., Wang, L., 2023. An implicit 3D nodal integration based PFEM (N-PFEM) of natural temporal stability for dynamic analysis of granular flow and landslide problems. Comput. Geotech. 159, 105434.
Zhou, W.-H., Tan, F., Yuen, K.-V., 2018. Model updating and uncertainty analysis for creep behavior of soft soil. Comput. Geotech. 100, 135–143.